Part one
Introduction

Advanced Characterization Techniques for Thin Film Solar Cells,
Edited by Daniel Abou-Ras, Thomas Kirchartz and Uwe Rau.

1
Introduction to Thin-Film Photovoltaics

Thomas Kirchartz and Uwe Rau

1.1
Introduction

From the early days of photovoltaics until today, thin-film solar cells have always competed with technologies based on single-crystal materials such as Si and GaAs. Owing to their amorphous or polycrystalline nature, thin-film solar cells always suffered from power conversion efficiencies lower than those of the bulk technologies. This drawback was and still is counterbalanced by several inherent advantages of thin-film technologies. Since in the early years of photovoltaics space applications were the driving force for the development of solar cells, the argument in favor of thin films was their potential lighter weight as compared with bulk materials.

An extended interest in solar cells as a source of renewable energy emerged in the mid-seventies as the limitations of fossil energy resources were widely recognized. For terrestrial power applications, the cost arguments and the superior energy balance strongly favored thin films. However, from the various materials under consideration in the fifties and sixties, only four thin-film technologies, namely amorphous hydrogen alloyed (a-)Si:H and the polycrystalline heterojunction systems CdS/Cu_xS, CdS/CdTe, and CdS/$CuInSe_2$, entered pilot production. Activities in the CdS/Cu_xS system stopped at the beginning of the eighties because of stability problems. At that time, amorphous silicon became the front runner in thin-film technologies keeping almost constantly a share of about 10% in a constantly growing photovoltaic market, the remaining 90% kept by crystalline Si. Despite their high-efficiency potential, polycrystalline heterojunction solar cells based on CdTe and $CuInSe_2$ did not play an economic role until to the turn of the century.

During the accelerated growth of the worldwide photovoltaic market in the first decade of new century, the three inorganic thin-film technologies increased their market share to 14%, where approximately 9% are covered by CdTe modules (numbers from 2008). With annual production figures in the GW range, inorganic thin-film photovoltaics has become a multibillion dollar business. In order to expand this position, further dramatic cost-reduction is required combined with a substantial increase in module efficiency. In this context, material and device

Advanced Characterization Techniques for Thin Film Solar Cells,
Edited by Daniel Abou-Ras, Thomas Kirchartz and Uwe Rau.

characterization becomes an important task not only for quality control in an expanding industry but also remains at the very heart of further technological progress.

This book concentrates on the three inorganic thin-film technologies – thin-film Si (a-Si:H combined with microcrystalline μc-Si:H to a tandem solar cell), and the two heterojunction systems CdS/CdTe as well as CdS/Cu(In,Ga)$(Se,S)_2$. These thin-film technologies have in common that they consist of layer sequences from disordered semiconductor materials that are deposited onto a supporting substrate or superstrate with the help of vacuum technologies. This layer structure and the use of disordered materials defines a fundamental difference to devices based on crystalline c-Si where a self-supporting Si wafer is transformed into a solar cell via a solid-state diffusion of dopant atoms. Thus, there are only the front and the back surface as critical interfaces in the classical wafer solar cell (with the notable exception of the a-Si:H/c-Si heterojunction solar cell). In thin-film solar cells, the number of functional layers can amount to up to eight and more. Some of these layers have thicknesses as low as 10 nm. In large-area modules, these layers homogenously cover areas of up to $6\,m^2$. These special features of the inorganic thin-film photovoltaic technologies define the field for the characterization techniques discussed in this book.

Electrical characterization, electroluminescence and photoluminescence, capacitance spectroscopy, and characterization of light trapping as considered in Chapters 2–5 and 7 are common photovoltaic analysis techniques. However, the specific properties of the thin-film systems like the disordered nature of the materials, the importance of features in the nm scale, and the fact that the film thicknesses are of the order or even in some cases much below the wavelength of visible light account for the special aspects that must be considered when using these techniques. Chapters 6, 8 and 9 deal with techniques like ellipsometry, the steady-state photocarrier grating method, and time-of-flight analysis that are specific thin-film methods some even invented within the field of thin-film photovoltaics. The following Chapters 10–17 discuss classical methods for material characterization, each of them having special importance for at least one of three technologies. Again, the specific features of photovoltaic thin films like the importance of dangling bonds and hydrogen passivation in disordered Si, the need for physical and chemical material analysis on the nanometer scale, or the prominence of interface chemistry and physics in thin-film solar cells define the focus of these chapters. Chapters 18–20 at the end of this handbook deal with the theoretical description of materials and devices. *Ab-initio* modeling of semiconductor materials is indispensable, because even the basic physical properties of some of the wide variety of compounds and alloys used in thin-film photovoltaics are not satisfactorily known. Finally, successful modeling of the finished devices may be looked at as the definitive proof of our understanding of materials and interfaces.

This introductory chapter yields a brief general introduction into the basic principles of photovoltaics highlighting the specific material and device properties that are relevant for the three thin-film technologies – a-Si:H/μc-Si:H, CdS/CdTe, and CdS/Cu(In,Ga)$(Se,S)_2$.

1.2
The Photovoltaic Principle

The temperature difference between the surface of the sun with a temperature of $T = 5800$ K and the surface of the earth ($T = 300$ K) is the driving force of any solar-energy conversion. Solar cells and solar modules directly convert the solar light into electricity using the internal photoelectric effect. Thus, any solar cell needs a photovoltaic absorber material that is not only able to absorb the incoming light efficiently but also to create mobile charge carriers, electrons, and holes, that are separated at the terminals of the device without significant loss of energy. Note that in *organic* absorber materials, most light-absorption processes generate excitons and a first step of charge separation is necessary in order to dissociate the exciton into free carriers. In contrast, the low binding energy of excitons in *inorganic* semiconductors makes absorption and generation of mobile charge carriers virtually identical in appropriate absorber materials of this type. Thus, after light absorption electrons and holes are present in the absorber and must be directed toward the two different contacts to the absorber, that is, the final charge carrier separation step.

For a semiconductor acting as a photovoltaic absorber, its band-gap energy E_g is the primary quantity defining how many charge carriers are generated from solar photons with energy $E \geq E_g$. Maximizing the number of photons contributing to the short-circuit current density of a solar cell would require minimizing E_g. Since photogenerated electron hole pairs thermalize to the conduction-band and valence-band edges after light absorption, the generated energy per absorbed photon corresponds to E_g regardless of the initial photon energy E. Thus, maximizing the band-gap energy E_g maximizes the available energy per absorbed photon. Therefore, one intuitively expects that an optimum band-gap energy exists between $E_g = 0$, maximizing the generated electron–hole pairs, and $E_g \rightarrow \infty$, maximizing the generated energy contained in a single electron–hole pair. Quantitatively, this consideration is reflected in the dependence of the maximum achievable conversion efficiency of a single band-gap photovoltaic absorber material as discussed in the following section.

1.2.1
The Shockley–Queisser Theory

The maximum power conversion efficiency of a solar cell consisting of single semiconducting absorber material with band-gap energy E_g is described by the Shockley–Queisser [1] (SQ) limit. In its simplest form, the SQ limit relies on four basic assumptions: (i) the probability for the absorption of solar light by the generation of a single electron–hole pair in the photovoltaic absorber material is unity for all photon energies $E \geq E_g$ and zero for $E < E_g$. (ii) All photogenerated charge carriers thermalize to the band edges. (iii) The collection probability for all photo-generated electron–hole pairs at short-circuit is unity. (iv) The only loss mechanism in excess of the nonabsorbed photons of (i) and the thermalization losses in (v) is the

spontaneous emission of photons by radiative recombination of electron–hole pairs as required by the principle of detailed balance.

In order to calculate the maximum available short-circuit current $J_{sc,SQ}$ as defined by (iii), we need the incoming photon flux ϕ_{inc} and the absorptance $A(E)$ defining the percentage of the incoming light at a certain photon energy E that is absorbed and not reflected or transmitted. The simplest approximation defined for an ideal absorber by condition (i) is a step-function, that is, $A(E) = 1$ (for $E > E_g$) and $A(E) = 0$ (for $E < E_g$). Then we have under short-circuit conditions (i.e., applied voltage $V = 0$ V)

$$J_{sc,SQ} = q \int_0^\infty A(E)\phi_{inc}(E)dE = q \int_{E_g}^\infty \phi_{inc}(E)dE \tag{1.1}$$

where q denotes the elementary charge.

Figure 1.1a compares the spectral photon flux corresponding to the terrestrial AM1.5G norm spectrum with the black body spectrum at $T = 5800$ K, both spectra normalized to a power density of 100 mW/cm^2. Figure 1.1b illustrates the maximum short-circuit current density that is possible for a given band-gap energy E_g according to Eq. (1.2).

Since light absorption by generation of free carriers and light emission by recombination of electron–hole pairs is interconnected by the principle of detailed balance, in thermodynamic equilibrium the emissivity ϕ_{em} is connected to the absorptance via Kirchhoff's law $\phi_{em} = A(E)\phi_{bb}(E, T)$, where $\phi_{bb}(E, T)$ is the black body spectrum at temperature T.

In a ideal solar cell under applied voltage bias, we use Würfel's generalization [2] of Kirchhoff's law to describe the recombination current $J_{rec,SQ}$ for radiative recombination according to

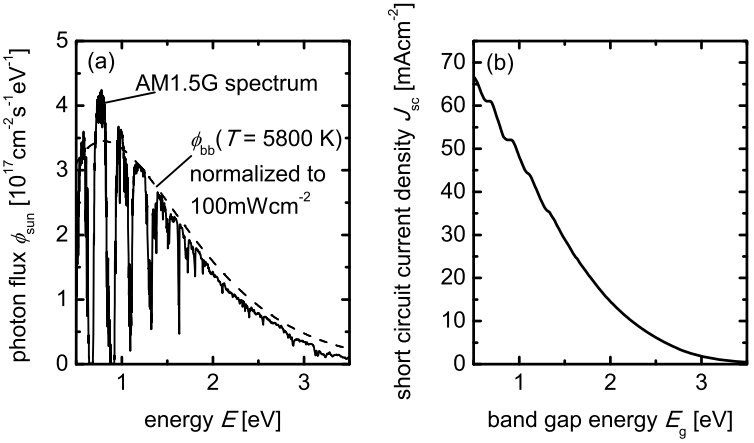

Figure 1.1 (a) Comparison of the AM1.5G spectrum with the black body spectrum of a body with a temperature $T = 5800$ K. Both spectra are normalized such that the power density is 100 mW/cm^2. (b) Using the AM1.5G spectrum and Eq. (2.1), we obtain the short-circuit current density $J_{sc,SQ}$ in the Shockley–Queisser limit as a function of the band-gap energy E_g of the solar absorber.

$$J_{\mathrm{rec,SQ}} = q\int_0^\infty A(E)\phi_{\mathrm{bb}}(E,T)\exp\left(\frac{qV}{kT}\right)dE = q\int_{E_g}^\infty \phi_{\mathrm{bb}}(E,T)\exp\left(\frac{qV}{kT}\right)dE \qquad (1.2)$$

where the second equality again results from the assumption of a sharp band-gap energy E_g. Thus, Eq. (1.2) describes the current density of a solar cell in the dark if only radiative recombination of carriers is considered corresponding to condition (iv) and the carriers have the temperature T of the solar cell according to condition (ii). The total current density J under illumination is a superposition of this radiative recombination current density and the short-circuit current density defined in Eq. (1.1). Thus, we can write

$$J(V) = J_{\mathrm{rec,SQ}}(V) - J_{\mathrm{sc,SQ}} = q\int_{E_g}^\infty \phi_{\mathrm{bb}}(E)dE\exp\left(\frac{qV}{kT}\right) - q\int_{E_g}^\infty \phi_{\mathrm{inc}}(E)dE \qquad (1.3)$$

There are two contributions to the incoming photon flux ϕ_{inc}, that is, the spectrum ϕ_{sun} of the sun and the photon flux ϕ_{bb} from the environment, which has the same temperature as the sample. When we replace the incoming photon flux ϕ_{inc} with the sum $\phi_{\mathrm{sun}} + \phi_{\mathrm{bb}}$, Eq. (1.3) simplifies to

$$J(V) = q\int_{E_g}^\infty \phi_{\mathrm{bb}}(E)dE\left[\exp\left(\frac{qV}{kT}\right) - 1\right] - q\int_{E_g}^\infty \phi_{\mathrm{sun}}(E)dE \qquad (1.4)$$

which is a typical diode equation with an additional photocurrent only due to the extra illumination from the sun. Now it is obvious that for zero excess illumination and zero volts applied, the current becomes zero.

Figure 1.2 shows the current density/voltage (J/V) curves of an ideal solar cell according to Eq. (1.4) for three different band-gap energies $E_g = 0.8$, 1.4, and 2.0 eV. If we evaluate Eq. (1.4) under open-circuit conditions, that is, at $J = 0$, we find the maximum possible voltage in the fourth quadrant of the coordinate system in Figure 1.2. This voltage is called the open-circuit voltage V_{oc} and follows from Eq. (1.4) as

$$V_{\mathrm{oc}} = \frac{kT}{q}\ln\left(\frac{\int_{E_g}^\infty \phi_{\mathrm{sun}}(E)dE}{\int_{E_g}^\infty \phi_{\mathrm{bb}}(E)dE} + 1\right) = \frac{kT}{q}\ln\left(\frac{J_{\mathrm{sc,SQ}}}{J_{0,\mathrm{SQ}}} + 1\right) \qquad (1.5)$$

Here, $J_{0,\mathrm{SQ}}$ is the saturation current density in the SQ limit, that is, the smallest possible saturation current density for a semiconductor of a given band gap. The open-circuit voltage increases nearly linearly with increasing band gap as shown in Figure 1.3a.

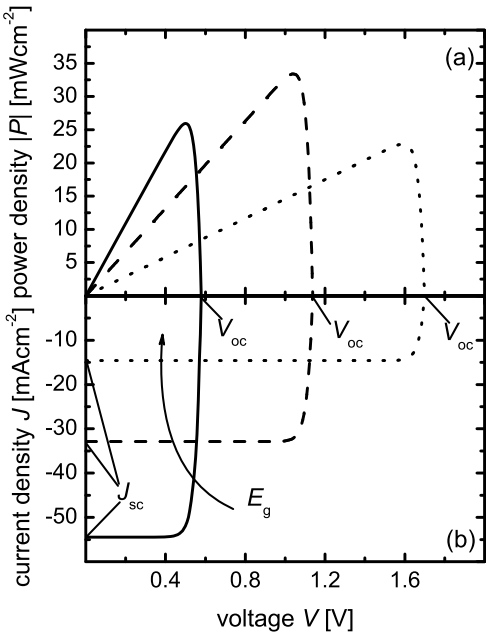

Figure 1.2 (a) Power density/voltage curves and (b) current density/voltage (J/V) curves of three ideal solar cells with band gaps $E_g = 0.8$, 1.4, and 2.0 eV, respectively. The higher the band gap E_g, the higher the open-circuit voltageV_{oc}, that is, the intercept of both power density and current density with the voltage axis. However, a higher band gap also leads to a decreased short-circuit current J_{sc} (cf. Figure 1.1b). The curves are calculated using Eq. (1.4).

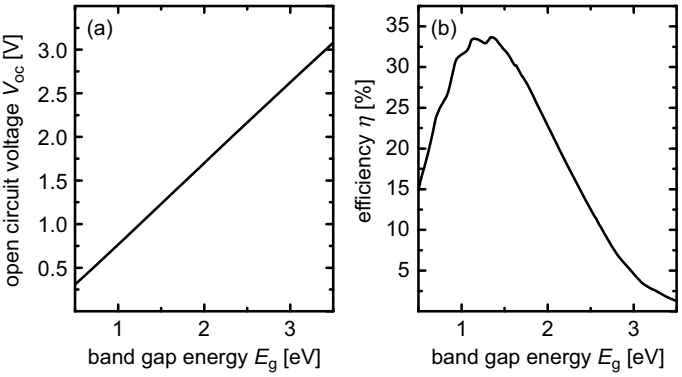

Figure 1.3 (a) Open-circuit voltage and (b) conversion efficiency as a function of the band-gap energy E_g in the Shockley–Queisser limit using an AM1.5G spectrum as illumination. The optimum band-gap energies for single junction solar cells are in the range of $1.1\,\text{eV} < E_g < 1.4\,\text{eV}$ with maximum conversion efficiencies around $\eta = 33\%$ under unconcentrated sunlight.

From Eq. (1.4), the power density follows by multiplication with the voltage. The efficiency η is then the maximum of the negative power density,[1)] that is,

$$\eta = \frac{-\max(J(V)V)}{P_{\text{opt}}} = \frac{-\max(J(V)V)}{\int_{E_g}^{\infty} E\phi_{\text{sun}}(E)dE} \tag{1.6}$$

Figure 1.3b shows the final result of the SQ theory: the efficiency as a function of the band-gap energy for illumination with the AM1.5G spectrum depicted in Figure 1.1a.

1.2.2
From the Ideal Solar Cell to Real Solar Cells

The universality and simplicity of the SQ limit is due to the fact that all internal details of the solar cell are irrelevant for its derivation. However, these hidden details are the practical subjects of research on real solar cells, and especially on thin-film solar cells. It is important to understand that some of these details idealized (or neglected) by the original SQ theory [1] are not in conflict with the detailed balance principle [3].

First, starting from a step-function like absorptance toward a more complex spectral dependence of $A(E)$ is not in conflict with the radiative recombination limit (cf. Eqs. (2.1) and (2.2)). A continuous transition from zero to unity is expected from any semiconductor material with finite thickness. Especially for thin-film absorbers, maximizing light absorption is an important task requiring additional means to confine the light as discussed in Section 1.2.3. Moreover, the disorder in thin-film absorbers may lead to additional electronic states close to the band gap (so-called band tails or band-gap fluctuations) with a considerable contribution to light absorption and emission. In consequence, the achievable conversion efficiency is reduced even in the radiative limit [4].

Second, proper extraction of the photogenerated electrons and holes requires sufficiently high carrier mobilities and selectivity of the contacts to make sure that all electrons and holes are collected in the n-type and in the p-type contact. Again, these requirements are valid even when restricting the situation to radiative recombination [5]. Since mobilities in disordered thin-film materials are generally lower than in mono-crystalline absorbers, charge carrier extraction is an issue to be discussed with especial care (Section 1.2.4).

Finally, recombination in thin-film solar cells is dominated by nonradiative processes. Thus, especially the achieved open-circuit voltages are far below the radiative limit. Section 1.2.5 and the major part of Chapter 2 will deal with understanding the efficiency limits resulting from all sorts of nonradiative recombination. It is important

1) Negative current density means here that the current density is opposite to the current density any passive element would have. A negative power density means then that energy is extracted from the device and not dissipated in the device as it would happen in a diode, which is not illuminated.

to note that even when considering nonradiative recombination, we must not necessarily abandon a detailed balance approach [6, 7] (cf. Chapter 3).

1.2.3 Light Absorption and Light Trapping

The first requirement for any solar cell is to absorb light as efficiently as possible. Solar-cell absorbers should, therefore, be nontransparent for photons with energy $E > E_g$. For any solar cell but especially for thin-film solar cells, this requirement is in conflict with the goal of using as little absorber material as possible. Additionally, thinner absorbers facilitate charge extraction for materials with low mobilities and/or lifetimes of the photogenerated carriers. This is why light trapping in photovoltaic devices is of major importance. Light trapping exploits randomization of light at textured surfaces or interfaces in combination with the fact that semiconductor absorber layers have typical refractive indices n that are much higher than that of air ($n = 1$) or glass ($n \approx 1.5$). Typical values for the real part of the refractive index are $n > 3.5$. But beforehand, the light has to enter the solar cell, and for the reflection at the front surface, a high refractive index is a disadvantage. The reflectance

$$R = \left(\frac{n-1}{n+1}\right)^2 \tag{1.7}$$

at the interface between air and the semiconductor will become higher when the refractive index gets higher. However, the high reflection at the front surface is reduced by using several layers between air and absorber layer. The refractive indices of these layers increase gradually, and any large refractive index contrast is avoided.

For light trapping, however, a high refractive index has an advantage. When the direction of the incoming light is randomized by a scattering interface somewhere in the layer stack of the thin-film solar cell, part of the light will be guided in the solar cell absorber by total internal reflection. The percentage of light kept in the solar cell by total internal reflection increases with the refractive index, since the critical angle $\theta_c = \arcsin(1/n)$ becomes smaller. For light with a Lambertian distribution of angles, the reflectance of the front surface for light from the inside is

$$R_i = 1 - \frac{(1-R_f)\int_0^{\theta_c} \cos\theta \sin\theta \, d\theta}{\int_0^{\pi/2} \cos\theta \sin\theta \, d\theta} = 1 - \frac{(1-R_f)}{n^2} \tag{1.8}$$

Here, R_f is the reflectance at the front side of the absorber for normal incidence.

To visualize the effect, the absorption coefficient and the light trapping has on the absorptance of a solar cell, we present some calculations for a model system. Let us assume a direct semiconductor, which have absorption coefficients of the typical form

$$\alpha = \alpha_0 \sqrt{(E - E_g)/1\,\text{eV}} \tag{1.9}$$

Then, the absorptance $A(E)$, that is, the percentage of photons that are absorbed and not reflected or transmitted at a certain photon energy, is calculated for flat

surfaces and for an absorber thickness much larger than the wavelength of light with

$$A = (1-R_f)\frac{\left(1-e^{-\alpha d}\right)\left(1+R_b e^{-\alpha d}\right)}{1-R_f R_b e^{-2\alpha d}} \tag{1.10}$$

Here, R_b is the reflectance at the backside. Equation (1.10) assumes an infinite number of reflections at the front and the back of the absorber layer. To calculate the real absorptance of any thin-film solar cell, it is rather useless for two reasons: (i) thin-film solar cells usually consist of not only one but several layers and (ii) the layer thicknesses are of the same order than the wavelength of light and interference cannot be neglected any more. Nevertheless Eq. (1.10) is useful to test the influence of the absorption coefficient on the absorptance. Figure 1.4a compares the absorptance calculated according to Eq. (1.10) for three different values of α_0, namely $\alpha_0 = 10^4, \sqrt{10} \times 10^4,$ and 10^5 cm^{-1}, and for a constant thickness d of the absorber of $d = 1$ μm. The reflectance at the front side is assumed to be $R_f = 0$ and the reflectance at the backside is $R_b = 1$.

To calculate the absorptance of textured cell with light trapping, it is necessary to integrate over all angles. The resulting equations are rather complicated [8, 9]; however, a simple and useful approximation exists for the case $R_b = 1$, namely [10]

$$A = \frac{1-R_f}{1+\dfrac{(1-R_f)}{4n^2\alpha d}} \tag{1.11}$$

Figure 1.4b shows the result of applying the absorption coefficient defined in Eqs. (1.9)–(1.11). Again, the absorptance for the case of perfect light trapping is calculated for $\alpha_0 = 10^4, \sqrt{10} \times 10^4,$ and 10^5 cm^{-1}, $d = 1$ μm, and $R_f = 0$. The refractive index is assumed to be $n = 3.5$. It is obvious that for a given value of α_0, the

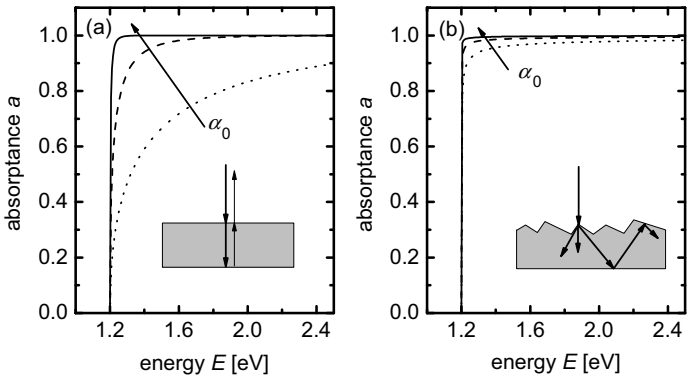

Figure 1.4 Absorptance as a function of photon energy for (a) a flat solar cell and (b) a textured solar cell with perfect light trapping. In both cases, the absorption coefficient α_0 from Eq. (1.9) is varied. The values are for both subfigures $\alpha_0 = 10^4, \sqrt{10} \times 10^4, 10^5$ cm^{-1}. For the same absorption coefficient, the textured solar cell has absorptances that are much closer to the perfect step function than the flat solar cell.

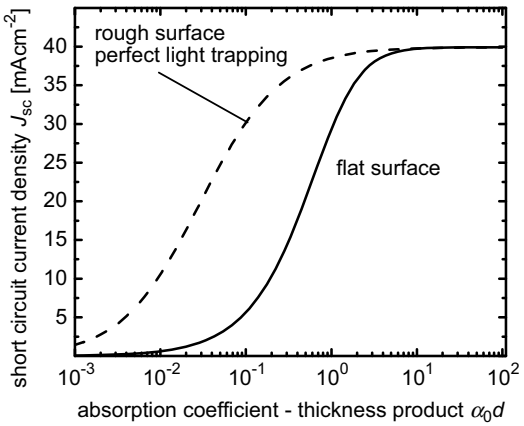

Figure 1.5 Comparison of the short-circuit current density of a flat (solid line) and a textured solar cell (dashed line) as a function of the product of α_0 and the thickness d assuming an absorption coefficient according to Eq. (1.9). Especially for low absorption coefficients relative to the device thickness (low $\alpha_0 d$), light trapping increases the short-circuit current density drastically. The refractive index used for these simulations is $n = 3.5$ independent of photon energy.

absorptance of the textured solar cell comes much closer to the perfect step-function like absorptance of the SQ limit.

To visualize the effect of light trapping on the short-circuit current density J_{sc}, Figure 1.5 compares the J_{sc} as a function of the product $\alpha_0 d$ for a flat and a Lambertian surface, that is, for absorptances calculated with Eqs. (1.10) and (1.11). The band gap is chosen to be $E_g = 1.2$ eV as in Figure 1.4 so the maximum J_{sc} for high $\alpha_0 d$ is the same as in the SQ limit (cf. Figure 1.1b), namely $J_{sc,max} = 40\,\mathrm{mA/cm^2}$. However, for lower $\alpha_0 d$, the J_{sc} with and without light trapping differ considerably and show the benefit from structuring the surface to enhance the scattering in the absorber layer. In reality, the benefit from light trapping will be smaller since the light has to be reflected several times at the front and especially at the back surface, where we assumed the reflection to be perfect. In reality any back reflector will absorb part of the light parasitically, that is, the light is absorbed but no electron–hole pairs are created, which could contribute to the photocurrent.

1.2.4
Charge Extraction

After an electron–hole pair is generated, the charge carriers must be extracted from the absorber layer. To get a net photocurrent, the electron must leave the device at the opposite contact than the hole. This requires a built-in asymmetry that makes electrons leave the device preferentially at the electron contact and holes at the hole contact.

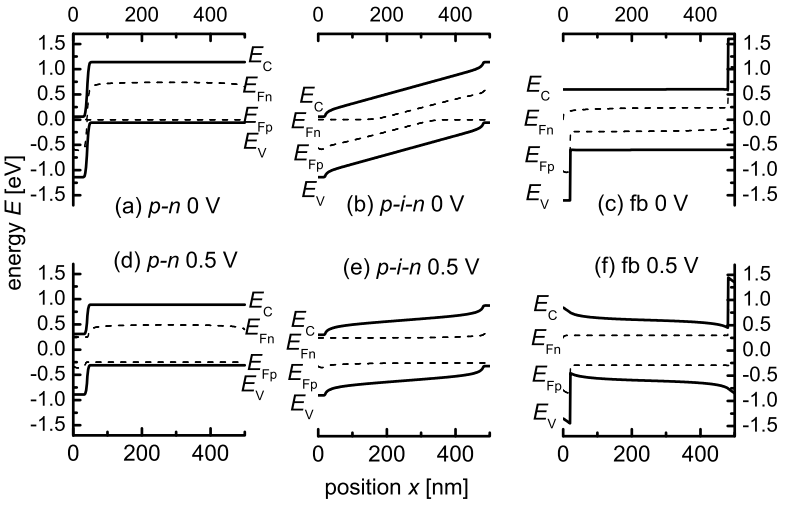

Figure 1.6 Simulation of the band diagrams of a (a, d) p–n-junction, a (b, e) p–i–n-junction, and a (c, f) flat-band (fb) solar cell under illumination. Every type of geometry is depicted under short-circuit conditions and under an applied forward bias $V = 0.5$ V.

Figure 1.6 introduces three device geometries that induce a built-in asymmetry that helps to extract oppositely charged carriers at opposite contacts. Figure 1.6a shows the band diagram of a p–n-junction solar cell under illumination and Figure 1.6d shows the same cell with an applied voltage $V = 0.5$ V. The simulations were done by solving the Poisson equation and the continuity equations with the software ASA, which is described in Chapter 19. As typical for most solar cells with a p–n-junction, the space charge region, where the bands are steep and the electric field is high, is at the very edge of the device. Most of the device consists, in our example, of a p-type base layer, where the field is practically zero. The transport of minority carriers (here electrons) to the space charge region is purely diffusive and independent from the applied voltage. That means application of a voltage does not change the electrical potential in the device, except for the space charge region.

The band bending at the junction leads to an asymmetry that separates the charges. Electrons are able to diffuse to the junction and then further to the n-type region and the electron contact. In addition, the p–n-junction serves as a barrier for holes which are in turn extracted by the back contact. Note that in the band diagram in Figure 1.6a and d, this back contact is not selective as is the p–n-junction. Therefore, also electrons can leave the device at this contact, a fact that is usually considered as contact recombination (cf. Chapter 2). Cu(In,Ga)Se_2 and CdTe solar cells are examples for p–n-(hetero)junctions.

For some disordered semiconductors like amorphous silicon, the electronic quality of doped layers is very poor. In addition, the mobilities and diffusion lengths are small, and thus purely diffusive transport would not lead to efficient charge extraction. The solution to this problem is the so-called p–i–n-junction diode. Here the doped layers are very thin compared to the complete thickness of the diode. The

largest share of the complete absorber thickness is occupied by an intrinsic, that is, undoped layer, in between the n and p-type regions. Figure 1.6a shows the band diagram of such a p–i–n-junction solar cell under illumination and Figure 1.6d shows the same cell with an applied voltage $V = 0.5$ V. Under short-circuit conditions, the region with a nonzero electric field extends over the complete intrinsic layer. Only directly at the contacts, the field is relatively small. When a forward voltage is applied to the cell, the electric field becomes smaller as shown in Figure 1.6d. Solar cells made from a-Si:H as well as a-Si:H/μc-SiH tandem cells use the p–i–n configuration.

Both p–n-junction and p–i–n-junction solar cells have a built-in field, meaning that the bands are bended due to the different conductivity type of the layers. Theoretically, such a band bending is not necessary to separate charges as can be shown by a gedanken experiment [11]. Figure 1.6c shows the band diagram of a hypothetical flat-band solar cell under short-circuit conditions. Like the p–i–n-junction solar cell, the flat-band solar cell has an intrinsic layer sandwiched between two other layers that induce the asymmetry for charge separation. In this case, the asymmetry is not due to band bending and differently doped layers but instead due to band offsets at the heterojunction between two materials with different band gaps. Let us assume we find one contact materials with zero band offset for the electrons and a high (in this case 1 eV) band offset for the holes and another material with the exact inverse properties. In this case, the band diagram is completely flat apart from the two band offsets. Like in the p–n-junction solar cell, the charge separation at short-circuit is arranged diffusive transport that is effective, when the diffusion length is high enough.

Under applied voltage, the drawback of the flat-band solar cell becomes obvious. The voltage has to drop somewhere over the absorber layer leading to an electric field, which is opposite to the direction the charge carriers should travel. While for a p–i–n-junction solar cell the field-assisted charge extraction becomes weaker with applied voltage, in a flat-band solar cell the field hinders charge separation. This is why we consider in the following the flat-band solar cell as a paradigmatic example for a device that exhibits poor charge separation properties. In fact, some typical features that show up in the numerical simulations below are indicative in practical (but faulty) devices for problems due to insufficient contact properties.

To illustrate the basic properties of the solar-cell structures introduced in Figure 1.6, we simulated the current/voltage curves for two different mobilities μ of electrons and holes. The recombination in the device was assumed to be dominated by one defect in the middle of the device with a Shockley–Read–Hall lifetime (see Section 1.2.5) $\tau = 100$ ns for electrons and holes. In addition, we assumed a surface recombination velocity $S = 10^5$ cm/s for the holes at the electron contact ($x = 0$) and the electrons at the hole contact ($x = 500$ nm). The results are presented in Figure 1.7a ($\mu = 10^{-1}\,\mathrm{cm^2/V\,s}$) and Figure 1.7b ($\mu = 10^{1}\,\mathrm{cm^2/V\,s}$) demonstrating that short-circuit current density is substantially decreased when turning from the high to the low mobility. The fill factor *FF*, that is,

$$FF = \frac{P_{\mathrm{mpp}}}{J_{\mathrm{sc}}\,V_{\mathrm{oc}}} \tag{1.12}$$

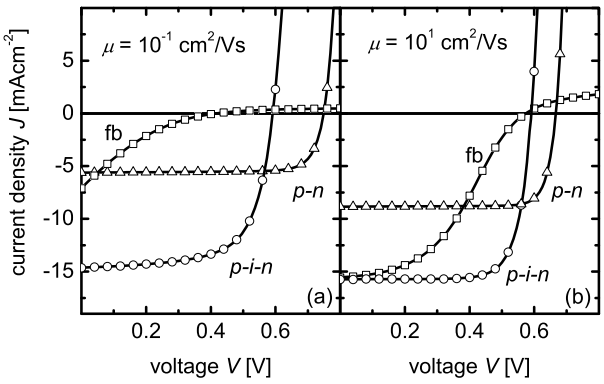

Figure 1.7 Simulated current/voltage curves of the three solar-cell geometries introduced in Figure 1.6 for two charge carrier mobilities, namely (a) $\mu = 10^{-1}\,\mathrm{cm}^2/\mathrm{V\,s}$ and (b) $\mu = 10^{1}\,\mathrm{cm}^2/\mathrm{V\,s}$. The main influence of a decreased mobility is a lower short-circuit current for the p–n-junction solar cell and a lower fill factor for the p–i–n-junction and the flat-band solar cell, which feature voltage-dependent charge carrier collection.

is for both cases relatively high. Here, P_{mpp} is the maximum power density that can be extracted from the device. Thus, the fill factor can be understood as the largest rectangle that fits between a J/V curve and the axis divided by the rectangle with the sides J_{sc} and V_{oc}.

For the p–n-junction solar cell, the open-circuit voltage also changes with mobility, which is due to increased surface recombination at high mobilities. This effect is relatively pronounced in this simulation since the complete thickness of the absorber is rather thin (500 nm) and the surface recombination velocity is assumed to be rather high ($S = 10^5\,\mathrm{cm/s}$). The same effect also explains the relatively low short-circuit current density of the p–n-junction geometry since there is no built-in field or heterojunction that keeps the minorities away from the "wrong" contact (at $x = 500$ nm in Figure 1.6). Thus, the p–n-junctions solar cell is relatively sensitive to the lack of selectivity of the back contact, that is, to surface recombination.

The p–i–n-junction has a much higher short-circuit current density changing also very little upon decrease in mobility from $\mu = 10^{1}\,\mathrm{cm}^2/\mathrm{V\,s}$ (Figure 1.7b) to $\mu = 10^{-1}\,\mathrm{cm}^2/\mathrm{V\,s}$ (Figure 1.7a). However, the fill factor decreases because of the reduced capability of the device to collect all charge carriers when under forward voltage bias the built-in field is reduced (cf. Figure 1.6e). This phenomenon is called bias-dependent carrier collection. Furthermore, the open-circuit voltage of the p–i–n-cell is lower than that of its p–n-type counterpart. Nevertheless, the p–i–n-structure delivers the highest output power under the assumed, unfavorable conditions, namely relative low carrier mobilities and high surface recombination velocities.

The flat-band solar cell has the most remarkable J/V curves. The J/V curves in both mobility cases are partly bended, leading to extremely low fill factors. This so-called S-shaped characteristic becomes more pronounced in the low-mobility case. Note that, in practice, such behavior is common to devices with faulty contacts and consequent insufficient carrier separation capabilities.

1.2.5
Nonradiative Recombination

The open-circuit voltage V_{oc} of any solar cell is considerably lower than its radiative limit, implying that nonradiative recombination mechanisms like Auger recombination [12] or recombination via defects, which is usually called Shockley–Read–Hall recombination [13, 14], dominate real-world devices. Figure 1.8 compares the three main recombination mechanisms. In case of radiative recombination (a), the excess energy of the recombining electron–hole pair is transferred to a photon. In case of (b) Auger recombination [15, 16], the excess energy serves to accelerate a third charge carrier (electron or hole), which thermalizes rapidly by emitting phonons. The third recombination mechanism is Shockley–Read–Hall recombination via states in the forbidden gap. Here, the excess energy is also transferred to phonons leading to an increase in the lattice temperature of the absorber.

In very high-quality devices from monocrystalline silicon, the recombination will be limited by Auger recombination and surface recombination. That means, even with a perfect bulk material without any defects, recombination in an indirect semiconductor like silicon will most likely not be limited by radiative recombination. However, typical thin-film solar cells are made from amorphous or microcrystalline semiconductors that are far from defect-free. Here, the most important recombination mechanism is recombination via states in the forbidden gap. These states can be for instance due to defects like dangling bonds [17] or due to band tails [18–20] arising from disorder in the material. Especially in amorphous Si, there is not only a single state in the band gap as indicated in Figure 1.8c but a complete distribution of

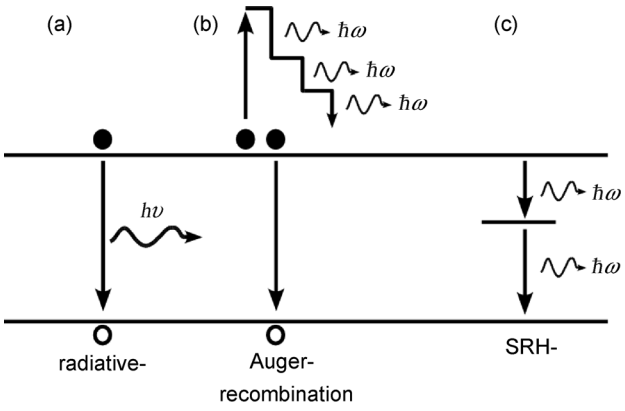

Figure 1.8 Overview over the three basic recombination mechanisms for photogenerated excess carriers in a semiconductor. The excess energy is either transferred to (a) a photon, (b) kinetic energy of an excess electron or hole, or (c) phonons. For case (b), the so-called Auger recombination, the kinetic energy of the electron is lost by collisions with the lattice, which heats up. In case (c), the emission of phonons becomes possible by the existence of states in the forbidden gap. This recombination mechanism is called Shockley–Read–Hall recombination.

states. The theory and modeling of such distributions of defects will be described later in Chapter 19, while we want to restrict ourselves here to some simple examples with a single defect state.

To visualize the influence of increased recombination rates on the current/voltage curve of solar cells, we made some numerical simulations using a very simple model for the recombination. This model assumes recombination via a defect in the middle of the forbidden gap, assuming capture cross sections σ for electrons and holes to be the same. Then the recombination rate according to Shockley–Read–Hall statistics is

$$R = \frac{np - n_i^2}{(n+p)\tau} \tag{1.13}$$

where τ is called the lifetime of the charge carrier. This lifetime depends on the density N_T of defect states, the capture cross section σ, and the thermal velocity v_{th} via

$$\tau = (v_{th}\sigma N_T)^{-1} \tag{1.14}$$

Figure 1.9 shows the current/voltage curves of a (a) p–i–n-junction solar cell and (b) a p–n-junction solar cell for a constant mobility $\mu = 1\,\mathrm{cm}^2/\mathrm{Vs}$ (for electrons and holes) and with a varying lifetime $\tau = 1\,\mathrm{ns}$, 10 ns, 100 ns, 1 μs, and 10 μs. All other parameters are defined in Table 1.1. It is important to note that a reduction in the lifetime has a different influence on the two geometries, which is in accordance with what we already observed when varying the mobility. For p–i–n-junction solar cells, a decrease in the lifetime leads to a decrease in open-circuit voltage, in fill factor, and in short-circuit current density. In contrast, the p–n-junction solar cell does not suffer from a decreased fill factor. The shape of the *J/V* curves stays practically the same. For low lifetimes (and/or low mobilities), the charge carrier collection in p–i–n-junction solar cells is voltage dependent. For p–n-junction solar cells, this is not the case. But

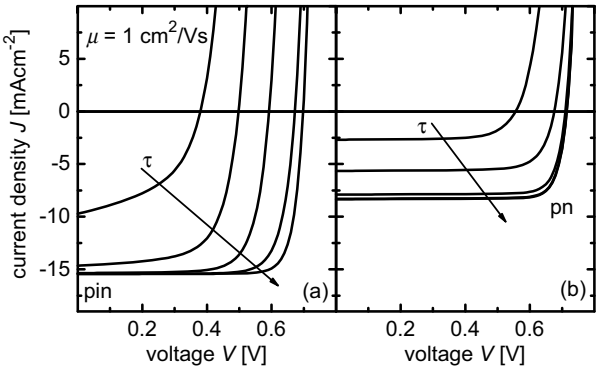

Figure 1.9 Current/voltage curves of (a) a p–i–n-junction solar cell and (b) a p–n-junction solar cell for a constant mobility $\mu = 1\,\mathrm{cm}^2/\mathrm{Vs}$ (for electrons and holes) and with a varying lifetime $\tau = 1\,\mathrm{ns}$, 10 ns, 100 ns, 1 μs, and 10 μs. All other parameters are defined in Table 1.1. An increasing lifetime helps to increase V_{oc} in both cases up to the level defined by the surface recombination alone. In case of the p–i–n-junction solar cell, the *FF* increases as well.

Table 1.1 Summary of all parameters for the simulations in this chapter that are not changed for the simulation[a)].

Parameters for all simulations in this chapter	Values
Band gap E_g	1.2 eV
Effective density of states N_C, N_V for conduction and valence band, respectively	$10^{20}\,cm^{-3}$
Doping concentrations N_D, N_A in all doped layers of p–n- and p–i–n-junction solar cells	$10^{19}\,cm^{-3}$
Total thickness d	500 nm
Generation rate G	$2 \times 10^{21}\,cm^{-3}\,s^{-1}$
Surface recombination velocity S	$10^{5}\,cm/s$

a) The mobilities and lifetimes, which are changed, are always given in the respective figure captions.

apart from the influence, the carrier lifetime has on charge extraction, which is very similar to the effect of the mobility; the lifetime has a pronounced influence on the open-circuit voltage. The increase in V_{oc} with increasing lifetime τ, however, seems not to follow a simple relation. For high values of τ, V_{oc} saturates for both p–i–n- and p–n-junction solar cells. This saturation is due to surface recombination, which limits the maximum attainable open-circuit voltage V_{oc}.

1.3 Functional Layers in Thin-Film Solar Cells

Until now, we have discussed the photovoltaic effect, the requirements for the material properties to come close to a perfect solar cell and the possible geometries to separate and extract charge carriers. In typical crystalline silicon solar cells, nearly all these requirements and tasks have to be fulfilled by the silicon wafer itself. Charge extraction is guaranteed by diffusing phosphorus into the first several hundred nanometers of the p-type wafer to create a p–n-junction. The wafer is texture etched to obtain a light trapping effect and to decrease the reflection at the front surface. The only additional layers that are necessary are the metal grid at the front, an antireflective coating (typically from SiN_x) and the metallization at the back.

Thin-film solar cells are usually more complex devices with a higher number of layers that are optimized for one or several purposes. In general, there are two configurations possible for any thin-film solar cell as shown in Figure 1.10. The first possibility is that light enters the device through a transparent superstrate. The superstrate has to maintain the mechanical stability of the device, while at the same time being extremely transparent. The superstrate is followed by layers which are part of the front contact, followed by the absorber layer and the layers that form the back contact. The second possibility is to inverse the layer stack, starting with the front contact, the absorber, and the back contact. These layers are all deposited on top of a substrate that is now not at the illuminated side of the device. Thus, the substrate can be transparent or opaque.

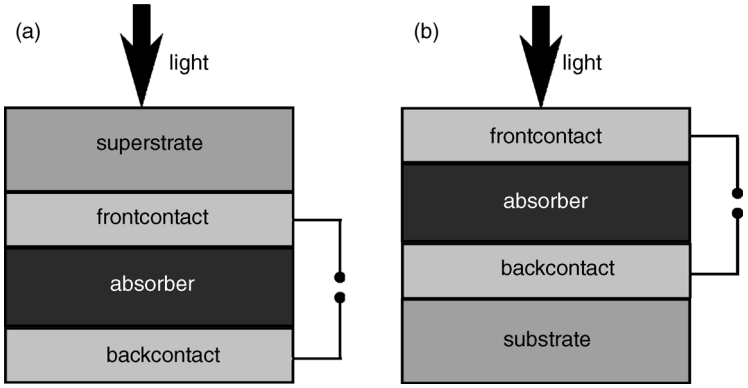

Figure 1.10 Sketch of the layer sequences to build up the system for thin-film solar cells in (a) superstrate and (b) substrate configuration. The minimum number of layers in excess of the supporting sub- or superstrate consists of the transparent and conductive front contact the absorber layer and the back contact.

Table 1.2 summarizes the roles and the requirement for the three functional layers and the sub/superstrate of thin-film solar cells. The substrate or superstrate provides mechanical stability. The functional layers are deposited onto the substrate or superstrate; thus it has to be thermally stable up to the highest temperature reached during the complete deposition process.

The front contact and back contact layers have to provide the electrical contact of the solar cell to the outside world, that is, the layers need high conductivities and must make a good electric contact to the absorber layers. In addition, the built-in field required for efficient charge extraction (especially at higher voltage bias) of a p–i–n-junction as depicted in Figure 1.6 requires doped contact layers. In devices that require efficient light trapping, usually the front and/or back contact layers are textured and have a lower refractive index than the absorber layer. Thus, the front contact layer additionally serves as an internal antireflective coating. In addition, a possible texture of the contact/absorber interface will lead to scattering of light and to increased path lengths of weakly absorbed light in the absorber layer. The back contact should have a high reflectivity so that weakly absorbed light is reflected multiple times.

Table 1.2 List of the four types of layers in a thin-film solar cell together with their specific tasks and requirements necessary for an efficient solar cell.

Layer type	Possible tasks and requirements
Substrate/superstrate	Mechanical and thermal stability, transparency (superstrate)
Front contact	Light trapping, antireflection, electrical contact, charge extraction
Absorber	Absorb light, charge extraction, low recombination
Back contact	Light trapping, high reflection, electrical contact, charge extraction

The absorber layer is central to the energy conversion process, requiring a steep rise of the absorption coefficient above the band gap, a high mobility and low recombination rates for efficient charge collection, and a high open-circuit voltage potential. In case of a p–n-junction device, the absorber layer must be moderately doped either intentionally or by intrinsic doping due to defects. In case of a p–i–n-junction device, the main absorber layer, the i-layer, should be undoped.

1.4 Comparison of Various Thin-Film Solar-Cell Types

The basic schemes of the layer stack of a thin-film solar cell, as presented in Figure 1.10, are implemented in different ways in the three most common inorganic thin-film technologies to date. These technologies are the $Cu(In,Ga)Se_2$ solar cell, the CdTe-based solar cell, and the thin-film silicon solar cell with amorphous and microcrystalline silicon absorbers. In the following, we will briefly discuss the main characteristics of these three technologies as well as the main challenges in future developments and how characterization of materials and devices can help to improve the devices. For those readers who desire a more detailed insight in the physics and technology of the different thin-film solar cells, we refer to a number of books and review articles on the topic. The physics and particularly the fabrication of all types of thin-film solar cells are discussed in Refs. [21–23], the physics of Cu-chalcopyrite solar cells in Ref. [24], the interfaces of CdS/CdTe solar cells in Ref. [25], the physics of amorphous hydrogenated silicon in Ref. [26], the physics and technology of thin-film silicon solar cells in Refs. [27–30], and the aspect of charge transport in disordered solids in Ref. [31].

1.4.1 $Cu(In,Ga)Se_2$

1.4.1.1 Basic Properties and Technology

Solar cells with an absorber layer made from $Cu(In,Ga)Se_2$ are currently the state of the art of the evolution of Cu-based chalcopyrites for use as solar cells. Heterojunctions between CdS and Cu_2S were the basis for first approaches for thin-film solar cells since the 1950s [32–35]. In 1974 first work on the light emission and light absorption of $CdS/CuInSe_2$ diodes was published [36–38]. While $CuInSe_2$ was not further considered for applications as a near-infrared light-emitting diode, its high absorption coefficient and electronically rather passive defects make it a perfect choice for use as a microcrystalline absorber material. Inclusion of Ga atoms on the In lattice site such that the ratio of Ga/(Ga + In) becomes around 20% shifts the band gap from 1.04 eV to around 1.15 eV, which is nearly perfect for a single-junction cell (cf. Figure 1.3). Today, thin-film solar cells with a $Cu(In,Ga)Se_2$ absorber layer are the most efficient thin-film technology with laboratory efficiencies up to 20% [39].

The classical layer stack for this type of solar cell is shown in Figure 1.11a. It consists of a typically 1 μm thick Mo layer deposited on a soda-lime glass substrate

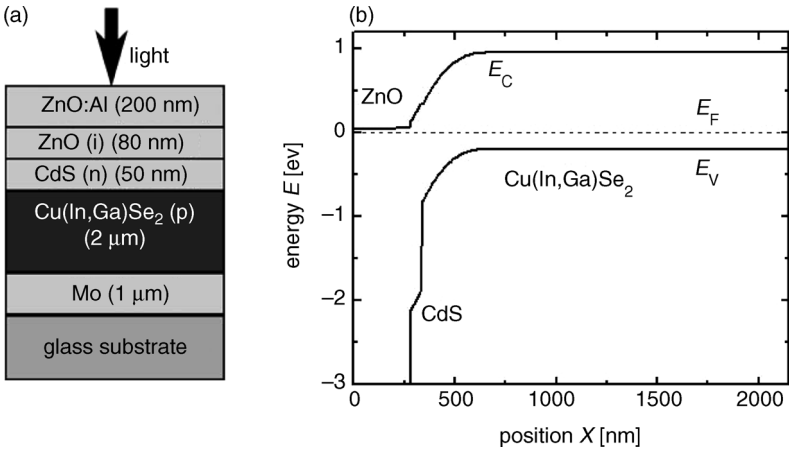

Figure 1.11 (a) Layer-stacking sequence and (b) energy band diagram of a typical ZnO/CdS/Cu(In, Ga)Se_2 heterojunction solar cell.

and serving as the back contact for the solar cell. Then, Cu(In,Ga)Se_2 is deposited on top of the Mo back electrode as the photovoltaic absorber material. This layer has a thickness of 1–2 μm. The heterojunction is then completed by chemical bath deposition (CBD) of CdS (typically 50 nm) and by the sputter deposition of a nominally undoped (intrinsic) *i*-ZnO layer (usually of thickness 50–70 nm) and then a heavily doped ZnO:Al window layer.

The Cu(In,Ga)Se_2 absorber material yielding the highest efficiencies is prepared by coevaporation from elemental sources. The process requires a maximum substrate temperature of ∼550 °C for a certain time during film growth, preferably toward the end of growth. Advanced preparation sequences always include a Cu-rich stage during the growth process and end up with an In-rich overall composition in order to combine the large grains of the Cu-rich stage with the otherwise more favorable electronic properties of the In-rich composition. The first example of this kind of procedure is the so-called Boeing or *bilayer process* [40], which starts with the deposition of Cu-rich Cu(In,Ga)Se_2 and ends with an excess In rate to achieve a final composition that is slightly In-poor. The most successful coeavaporation process is the so-called *three-stage process* [41] where first $(In,Ga)_2Se_3$ (likewise In, Ga, and Se from elemental sources to form that compound) is deposited at a lower temperatures (typically around 300 °C). Then Cu and Se are evaporated at an elevated temperature and finally again In, Ga, and Se to ensure the overall In-rich composition of the film even if the material is Cu-rich during the second stage.

The second class of absorber preparation routes is based on the separation of deposition and compound formation into two different processing steps. High efficiencies are obtained from absorber prepared by selenization of metal precursors in H_2Se [42] and by rapid thermal processing of stacked elemental layers in an Se atmosphere [43]. These sequential processes have the advantage that approved large-area deposition techniques such as sputtering can be used for the deposition of the

materials. The $Cu(In,Ga)Se_2$ film formation then requires a second step, the selenization step typically performed at similar temperatures as the coevaporation process. Both absorber preparation routes are now used in industrial application.

Important for the growth of the $Cu(In,Ga)Se_2$ absorber is the active role of Na during absorber growth. In most cases, the Na comes from the glass substrate and diffuses into the absorber [44]. But there are also approaches where Na is incorporated by the use of Na-containing precursors [45, 46]. The explanations for the beneficial impact of Na are manifold, and it is most likely that the incorporation of Na in fact results in a *variety* of consequences (for a review see Ref. [47]).

1.4.1.2 Layer-Stacking Sequence and Band Diagram of the Heterostructure

Figure 1.11 displays the layer-stacking sequence (a) and the band diagram of the $ZnO/CdS/Cu(In,Ga)Se_2$ heterojunction (b). The back contact consists of a sputtered Mo layer. In excess of producing a functional, conductive contact, proper preparation of this layer is also important for adhesion of the absorber film and, especially, for the transport of Na from the glass substrate through the Mo layer into the growing absorber. A homogeneous and sufficient supply of Na depends much on the microstructure of this layer. In contrast, if Na is supplied from a precursor additional blocking layers prevent out-diffusion of Na from the glass. Quantitative chemical depth profiling as described in Chapter 16 is a decisive tool to shed more light into the role of Na and on its way how it is functional during absorber growth.

The $Cu(In,Ga)Se_2$ absorber material grown on top of the Mo contact is slightly p-type doped by native, intrinsic defects, most likely Cu-vacancies [48]. However, the net doping is a result of the difference between the acceptors and an almost equally high number of intrinsic donors [49, 50]. Thus, the absorber material is a highly compensated semiconductor. Furthermore, the material features electronic metastabilities like persistent photoconductivity [51], which are theoretically explained by different light-induced defect relaxations [52]. However, final agreement on the observed metastability phenomena has not yet achieved, leaving an urgent need for further theoretical and experimental access to the complex defect physics of $Cu(In,Ga)Se_2$ (for a review of the present status, see Ref. [48]). Some experimental and theoretical methods helpful for further research are outlined in Chapters 7 and 18 of this book.

Another puzzle is the virtual electronic inactivity of most grain boundaries in properly prepared polycrystalline $Cu(In,Ga)Se_2$ absorbers being one essential ingredient for the high photovoltaic efficiencies delivered by this material. A discussion of the present status is given in Ref. [53]. A great part of the structural analysis methods discussed in this book (Chapters 11–14) describes tools indispensable for a better understanding of the microstructure of the $Cu(In,Ga)Se_2$ absorber material.

The surface properties of $Cu(In,Ga)Se_2$ thin films are especially important, as this surface becomes the active interface of the completed solar cell. The free surface of as-grown $Cu(In,Ga)Se_2$ films exhibits a very unique feature, namely a widening of the band gap with respect to the bulk of the absorber material [54, 55]. This band-gap widening results from a lowering of the valence band and is effective in preventing interface recombination at the absorber buffer interface [56, 57]. This surface layer

has an overall Cu-poor composition and a thickness of 10–30 nm [58]. Understanding the interplay between this surface layer and the subsequently deposited buffer layer is one of the decisive challenges for the present and future research.

The 50 nm thick CdS buffer layer is in principle too thin to complete the heterojunction. In fact the role of the CdS buffer in the layer system is still somewhat obscure. It is however clear that the undoped (i) ZnO layer is also a vital part of a successful buffer/window combination. Furthermore, both interfaces of the CdS interlayer to the Cu(In,Ga)Se_2 absorber and to the (i) ZnO play a vital role [59]. Under standard preparation conditions, the alignment of the conduction bands at both interfaces is almost flat [60] such that neither barrier for electron transport occurs nor is the band diagram distorted in a way to enhance interface recombination. However, it turns out that a replacement of CdS by a less cumbersome layer is not straightforward. Although while promising materials like In(OH,S), Zn(OH,S), In_2Se_3, ZnSe, ZnS (for an overview see Ref. [61]) mostly in combination with standard ZnO double layer have been investigated in some detail, no conclusive solution has been found despite reported efficiencies of 18% using ZnS buffer layers [62]. Recent research [63] focuses at combinations of Zn(S,O,OH)/ZnMgO replacing the traditional CdS/(i) ZnO combination. Alternative buffer layers like ZnS also have the advantage of a higher band-gap energy $E_g = 3.6$ eV compared to that of CdS $E_g = 2.4$ eV. By the higher E_g, parasitic absorption in the buffer layer is restricted to a much narrower range and the short circuit current density in Cd-free cells can exceed that of standard devices by up to 3 mA/cm^2 [63]. However, all technological improvements rely on our scientific understanding of the physics, chemistry, and microstructure of the heterointerfaces involved in the solar cell. Surface analysis methods as those discussed in Chapters 13 and 15 have already contributed much to our present knowledge and provide the promise to deepen it further.

1.4.2 CdTe

1.4.2.1 Basic Properties and Technology

Just as the CdS/Cu(In,Ga)Se_2 solar cell, also the CdS/CdTe devices are descendants of the first CdS/Cu_2S solar cells. In the mid-1960s, first experiments with tellurides were performed. Efficiencies between 5% and 6% were obtained for CdTe/$CuTe_2$ devices [64, 65]. Since Cu diffusion led to instabilities in these devices, instead CdS and CdTe were combined to form a p–n-heterojunction with efficiencies around 6% [66]. Thirty years later, the efficiency has increased to above 16% [67]. In addition, CdTe solar modules represent the by far most successful photovoltaic thin-film technology with a share of almost 10% in the global photovoltaic market (data from 2008).

One decisive reason for this success is the relative ease which with CdTe solar cells and modules are prepared. Several types of transparent conductive oxides (TCO) are used as front contact materials for the preparation of CdTe solar cells, SnO_2:F and In_2O_3:F being the most common ones. Both materials, CdS and CdTe, forming the heterojunction of the solar cell, are grown with similarly fast and reliable methods,

including closed-space sublimation, spraying, screen printing followed by sintering, and electrodeposition. Since CdS grows natively as n-type and CdTe as p-type material, the p–n-heterojunction forms automatically.

However, in order to improve the device efficiency substantially, an additional step, the $CdCl_2$-activation, is necessary. A vapor-based approach is most useful with regard to industrial applications [68]. The activation step leads to an intermixing of CdS and CdTe close to the heterointerface and to the formation of a Cu(Te,S) compound. In some cases, recrystallization of the CdTe film was observed after $CdCl_2$ treatment [69]. In any case, the intermixing process is decisive for the improvement of the device performance.

The major challenge for reliable manufacture of efficient devices is to produce a stable and ohmic back contact to the CdTe absorber with its high electron affinity. Often, back contacts are made with materials that contain Cu, such as Cu_2Te, ZnTe:Cu, or HgTe:Cu, enabling a relatively low contact resistance. However, Cu-diffusion in CdTe is fast and extends deeply into the absorber, thereby affecting considerably the stability of the device [70]. Cu-free alternative contact materials embrace, for example, Sb_2Te_3 [71]. Often, an etching step is used to produce a Te-rich interlayer, providing higher p-type doping and, consequently, a reasonably low-ohmic contact [72].

1.4.2.2 Layer-Stacking Sequence and Band Diagram of the Heterostructure

From the point of view of the layer-stacking sequence and the band diagram shown in Figure 1.12a and b, the CdS/CdTe heterostructure is quite similar to those of the CdS/Cu(In,Ga)Se_2 heterostructure given in Figure 1.11. One obvious difference is the low doping density of the CdTe absorber, making the device somewhat a hybrid between a p–i–n- and a p–n-junction. The built-in field almost stretches from the heterointerface toward the back contact. As we have already seen, such a configuration is helpful

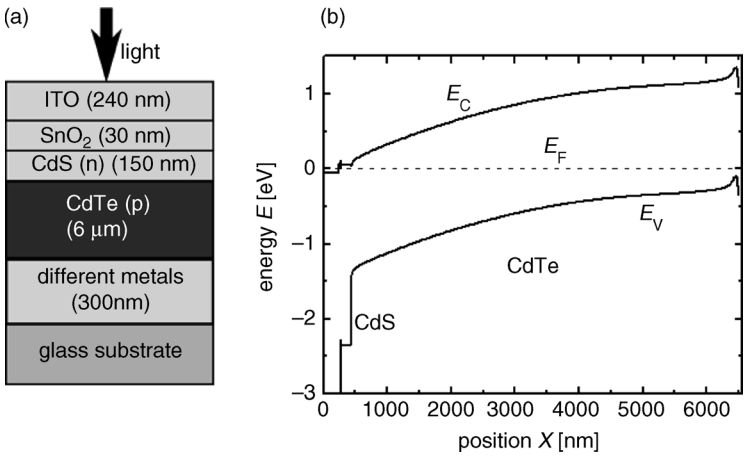

Figure 1.12 (a) Layer stacking sequence and (b) energy-band diagram of a typical CdTe-based solar cell following Ref. [73].

for carrier collection but has the drawback of delivering lower open circuit voltages than a p–n-type device with a relatively narrow space charge region.

The band diagram at the back contact features a highly p-doped region due to Cu-indiffusion or due to the formation of a Te-rich interlayer. This leads to a relatively thin yet high barrier for holes. Thus, the electrical contact is achieved via tunneling from the absorber into the back metal. The modeling of CdTe solar cells, including a proper approach to the back contact, which usually is by far not perfectly ohmic, represents a major challenge as discussed in Chapter 19.

The average grain sizes in the polycrystalline CdTe absorbers range from 1 to 2 mm, thus somewhat larger than in Cu(In,Ga)Se_2. However, the grain boundaries are considerably more electronically active than in Cu(In,Ga)Se_2. For instance, photocurrent concentration along grain boundaries [74] indicates type inversion of grain boundaries in CdTe. This could be helpful for current collection (along the grain boundaries) but also implies losses for the open circuit voltage. Again, connecting microstructural analysis with highly resolved measurements of electronic properties by scanning techniques as described in Chapters 11 and 12 will clarify the picture in the future.

The favorable, flat conduction band alignment at the CdTe/CdS as well as at the CdS/TCO interface as featured by Figure 1.12b is similar to the situation for Cu(In, Ga)Se_2 devices. In CdTe solar cells this is basically a result of the $CdCl_2$ activation process and of intermixing [73].

1.4.3
Thin-Film Silicon Solar Cells

1.4.3.1 Hydrogenated Amorphous Si (a-Si:H)

Central to the working principle of semiconductors is the forbidden energy gap derived from the periodicity of the crystal lattice. However, it is exactly this strict periodicity that is lacking in amorphous semiconductors, which have a short-range order but no long-range order as their crystalline counterparts. The structural disorder caused by variations in bond lengths and angles has several implications for the electronic and optical properties of amorphous materials. The most important feature is the peculiar density of electronic states in amorphous silicon featuring localized states close to the band edges that arise from disorder and a distribution of deep states due to unpassivated, that is, dangling, bonds. In addition the word band gap is no longer adequate in amorphous semiconductors. Instead, an optical gap is defined from the onset of absorption, while a mobility gap is defined as the approximate demarcation line between localized and extended states [75]. Despite the fact that the mobility gap is not a forbidden zone for electrons but instead full of localized states, amorphous silicon still proves to be a useful material for thin-film devices like solar cells, photodetectors, and transistors [76].

While first crystalline silicon solar cells with reasonable efficiencies of about $\eta = 6\%$ were already developed in 1954 [77], the research on amorphous silicon first needed two breakthroughs before the fabrication of the first amorphous silicon solar cells in 1976 became possible [78]. The first breakthrough was the realization that the

addition of considerable amounts of hydrogen helped to passivate dangling bonds in the amorphous material thereby leading to sufficiently low defect densities that hydrogenated amorphous silicon showed some of the important characteristics of useful semiconductors like dopability and photoconductivity [79]. The second breakthrough was the successful doping of amorphous silicon [80].

Despite the defect passivation with hydrogen, the defect densities in a-Si:H are still relatively high with diffusion lengths between 100 and 300 nm [81]. In doped a-Si:H layers, the defect density is two or three orders of magnitude higher and the diffusion length is accordingly even lower. Thus, a p–n-junction as used in crystalline silicon but also in Cu(In,Ga)Se_2 as well as CdTe solar cells would not work for a-Si:H, since the diffusion length is too low. Since the absorber thickness cannot be made much thinner than the diffusion length due to the large losses because of insufficient light absorption, a p–i–n-junction configuration has to be used. The first advantage is that most of the absorber layer consists of intrinsic a-Si:H with its higher carrier lifetime than doped a-Si:H. The second advantage is that the built-in field helps with extracting charge carriers as shown in Figure 1.13. The advantage of the p–i–n-configuration is that the electron and hole concentrations are similar in a relatively large portion of the absorber volume, which increases defect recombination, which is automatically highest, when electron and hole concentrations are equal.

Figure 1.13 shows the typical layer stack and band diagram of an a-Si:H p–i–n-type solar cell. Usually a superstrate configuration is used, although a substrate configuration is also possible. In the latter case, the solar cell is deposited on the substrate starting with the back contact and the n-type layer. Thus, such a solar cell is called nip

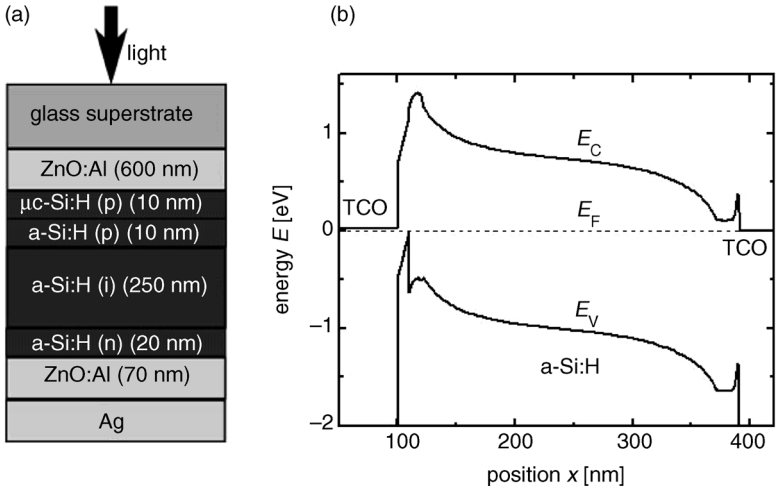

Figure 1.13 (a) Stacking sequence and (b) band diagram of a typical a-Si:H p–i–n solar cell. The main absorber layer is intrinsic while the built-in field is due to the thin doped silicon layers. Due to the asymmetric mobilities between electrons and holes, the p-type layers will always be on the illuminated side, ensuring that the holes with their lower mobility have the shorter way to the contacts.

solar cell, where n–i–p represents the deposition order. In both cases of a substrate or superstrate configuration, the illumination is always from the p-side. This is due to the lower mobility of holes in a-Si:H. It is therefore beneficial to have the hole contact on the illuminated side, where the generation rate is higher. With the hole contact on the illuminated side, the distance the slowest carrier has to travel to the contacts is minimized.

1.4.3.2 Metastability in a-Si:H: The Staebler–Wronski Effect

Shortly after the first reports on a-Si:H solar cells, Staebler and Wronski published their findings on metastability in a-Si:H [82]. Under illumination, the conductivity of a-Si:H degrades but can be restored by annealing at temperatures of about 425 K. This degradation effect is known as the Staebler–Wronski effect (SWE). The metastable behavior is ascribed to the light-induced creation of additional defects. It is generally accepted that these metastable defects are additional dangling bonds that act like recombination centers in the material and that these dangling bonds are created by the breaking of weak or strained Si−Si bonds. Hydrogen plays an important role in the metastable behavior of a-Si:H; however, there is no consensus on the exact mechanisms involved and the role of hydrogen in the SWE [83–86]. The creation of additional recombination centers affects a-Si:H-based solar cells to such a degree that the SWE is a severe limitation for the application of a-Si:H in single-junction solar cells.

1.4.3.3 Hydrogenated Microcrystalline Silicon (μc-Si:H)

As can be seen by comparison with Figure 1.3b, the high optical gap of a-Si:H of approximately 1.75 eV (the exact value depending on the definition and on the hydrogen content) is too high for a single-junction solar cell. It was, therefore, an important discovery in thin-film silicon solar-cell research to find a way to prepare hydrogenated microcrystalline silicon (μc-Si:H) with approximately the same band gap as crystalline silicon (E_g (c-Si) = 1.12 eV) that had a sufficient quality for use in solar cells. First μc-Si:H layers were deposited in the 1960s [87] and successful doping in the 1970s [88]. However, the material had insufficient electronic quality for use in solar cells. The use of gas purifiers in the 1990s by the Neuchâtel group made the fabrication of μc-Si:H layers with sufficiently low oxygen contents [89–91] and the successful fabrication of first μc-Si:H solar cells with reasonable efficiencies possible [92, 93].

1.4.3.4 Micromorph Tandem Solar Cells

One possibility to overcome [94] the efficiency limit of SQ is the use of a multijunction solar cell with absorber layers having different band gaps. The highest band-gap absorber should be on the illuminated side such that all high-energy photons are absorbed by the absorber with the higher band gap and the low-energy photons are absorbed by the cell or the cells with the lower band gap(s). If every absorber has its own p–n- or p–i–n-junction, then they can be deposited on top of each other such that one obtains two or more series connected solar cells on top of each other. This approach minimizes the losses due to thermalization of carriers and due to the

transparency of any solar cell for photons with energies below the band gap of the absorber. With a similar approach as discussed in Section 1.1, the efficiency [95] and the optimal band-gap combinations can be calculated for multijunction solar cells in general and tandem (i.e., two-junction solar cells) in particular [96, 97]. It is a fortunate coincidence that the optimum combination for a tandem solar cell is close to the actual band gaps of amorphous (E_g (a-Si:H) ≈ 1.75 eV) and microcrystalline silicon (E_g (μc-Si:H) ≈ 1.2 eV). Although in principle efficiencies above the SQ limit for single-junction solar cells are possible with such a configuration, in reality the efficiencies are much lower than the SQ limit and even lower than efficiencies of real crystalline Si single-junction solar cells. Nevertheless, the tandem cell made from a-Si:H and μc-Si:H has achieved slightly higher efficiencies than either of the single-junction devices (see Ref. [29] for an overview). For these thin-film tandem cells with their relatively low mobilities, a second motivation arises for the use of tandem solar cells. Since the built-in field decreases for increasing thickness and since the charge collection becomes increasingly difficult with increasing distance to the contacts, thin solar cells have higher fill factors than thicker solar cells. The tandem approach is a useful way to keep individual cell thicknesses low and at the same time have a higher total thickness and a better absorptance.

1.5 Conclusions

Despite more than 30 years of research invested in each of the three thin-film solar-cell technologies considered here, a large series of questions has still to be answered. The need for more "know-why" in addition to the available "know-how" is urged by the responsibility of scientists toward a steadily growing industry and toward a world in need for clean energy. Fortunately, more and more specialists for sophisticated physical and chemical analysis methods enter the field and help improving our common understanding as well as improving our technology. The most satisfying answers always will arise from a combination of a solid understanding of the photovoltaic principles with the results from various methods analyzing the electronic, chemical, and structural properties of all the layers and interfaces in the device.

References

1 Shockley, W. and Queisser, H.J. (1961) Detailed balance limit of efficiency of p–n junction solar cells. *J. Appl. Phys.*, **32**, 510.

2 Würfel, P. (1982) The chemical potential of radiation. *J. Phys. C*, **15**, 3967–3985.

3 Bridgman, P.W. (1928) Note on the principle of detailed balancing. *Phys. Rev.*, **31**, 101.

4 Rau, U. and Werner, J.H. (2004) Radiative efficiency limits of solar cells with lateral band-gap fluctuations. *Appl. Phys. Lett.*, **84**, 3735–3737.

5 Mattheis, J., Werner, J.H., and Rau, U. (2008) Finite mobility effects on the radiative efficiency limit of pn-junction solar cells. *Phys. Rev. B*, **77**, 085203.

6 Rau, U. (2007) Reciprocity relation between photovoltaic quantum efficiency and electroluminescent emission of solar cells. *Phys. Rev. B*, **76**, 085303.

7 Kirchartz, T. and Rau, U. (2008) Detailed balance and reciprocity in solar cells. *phys. status solidi (a)*, **205**, 2737–2751.

8 Green, M.A. (2002) Lambertian light trapping in textured solar cells and light-emitting diodes: analytical solutions. *Prog. Photovolt. Res. Appl.*, **10**, 235.

9 Mattheis, J. (2008) Mobility and homogeneity effects on the power conversion efficiency of solar cells, Dissertation, Universität Stuttgart, http://elib.uni-stuttgart.de/opus/volltexte/2008/3697/ (23.2.2010).

10 Tiedje, T., Yablonovitch, E., Cody, G.D., and Brooks, B.G. (1984) Limiting efficiency of silicon solar cells. *IEEE Trans. Electron Devices*, **ED-31**, 711.

11 Würfel, P. (2002) *Physica E*, **14**, 18–26.

12 Green, M.A., Limits on the open-circuit voltage and efficiency of silicon solar cells imposed by intrinsic auger processes. *IEEE Trans. Electron Devices*, **ED-31**, 671.

13 Hall, R.N. (1952) Electron–hole recombination in germanium. *Phys. Rev.*, **87**, 387.

14 Shockley, W. and Read, W.T. (1952) Statistics of the recombinations of holes and electrons. *Phys. Rev.*, **87**, 835.

15 Auger, P. (1925) Sur L'effet photoélectrique composé. *J. Physique et Le Radium*, **6**, 205.

16 Meitner, L. (1922) Über die β-Strahl-Spektra und ihren Zusammenhang mit der γ-Strahlung. *Zeitschrift für Physik A Hadrons and Nuclei.*, **11**, 35.

17 Dersch, H., Stuke, J., and Beichler, J. (1981) Light-induced dangling bonds in hydrogenated amorphous silicon. *Appl. Phys. Lett.*, **38**, 456.

18 Tiedje, T., Cebulka, J.M., Morel, D.L., and Abeles, B. (1981) Evidence for exponential band tails in amorphous silicon hydride. *Phys. Rev. Lett.*, **46**, 1425.

19 Schiff, E.A. (1981) Trap-controlled dispersive transport and exponential band tails in amorphous silicon. *Phys. Rev. B*, **24**, 6189.

20 Fedders, P.A., Drabold, D.A., and Nakhmanson, S. (1998) Theoretical study on the nature of band tail states in amorphous Si. *Phys. Rev. B*, **58**, 15624.

21 Poortmans, J. and Arkhipov, V. (eds) (2006) *Thin Film Solar Cells – Fabrication, Characterization and Applications*, John Wiley & Sons, Ltd, Chichester, UK.

22 Hamakawa, Y. (ed.) (2004) *Thin-Film Solar Cells: Next Generation Photovoltaics and Its Applications*, Springer, Berlin.

23 Chopra, K.L., Paulson, P.D., and Dutta, V. (2004) Thin-film solar cells: An overview. *Prog. Photovolt. Res. Appl.*, **12**, 69.

24 Siebentritt, S. and Rau, U. (eds) (2006) *Wide-Gap Chalcopyrites*, Springer, Berlin.

25 Jaegermann, W., Klein, A., and Mayer, T. (2009) Interface engineering of inorganic thin-film solar cells – materials-science challenges for advanced physical concepts. *Adv. Mater.*, **21**, 4196.

26 Street, R.A. (1991) *Hydrogenated Amorphous Silicon*, Cambridge University Press, Cambridge.

27 Zeman, M. and Schropp, R.E.I. (1998) *Amorphous and Microcrystalline Silicon Solar Cells: Modeling, Materials and Device Technology*, Kluwer Academic Publishers, Norwell.

28 Shah, A.V., Schade, H., Vanecek, M., Meier, J., Vallat-Sauvain, E., Wyrsch, N., Kroll, U., Droz, C., and Bailat, J. (2004) Thin-film silicon solar cell technology. *Prog. Photovolt. Res. Appl.*, **12**, 113.

29 Schropp, R.E.I., Carius, R., and Beaucarne, G. (2007) Amorphous silicon, microcrystalline silicon, and thin-film polycrystalline silicon solar cells. *MRS Bull.*, **32**, 219.

30 Deng, X. and Schiff, E.A. (2003) Amorphous Silicon-based solar cells, in *Handbook of Photovoltaic Science and Engineering* (eds A. Luque and S. Hegedus) John Wiley & Sons Ltd, Chichester, UK, p. 505.

31 Baranovski, S. (ed.) (2006) *Charge Transport in Disordered Solids – with Applications in Electronics*, John Wiley & Sons, Ltd, Chichester, UK.

32 Reynolds, D.C., Leies, G., Antes, L.L., and Marburger, R.E. (1954) Photovoltaic effect in cadmium sulfide. *Phys. Rev.*, **96**, 533.

33 Böer, K.W. (1976) Photovoltaic effect in CdS–Cu_2S heterojunctions. *Phys. Rev. B*, **13**, 5373.

34 Böer, K.W. and Rothwarf, A. (1976) Materials for solar photovoltaic energy conversion. *Annu. Rev. Mater. Sci.*, **6**, 303.

35 Pfisterer, F. (2003) The wet-topotaxial process of junction formation and surface treatments of Cu_2S–CdS thin-film solar cells. *Thin Solid Film.*, **431–432**, 470.

36 Migliorato, P., Tell, B., Shay, J.L., and Kasper, H.M. (1974) Junction electroluminescence in $CuInSe_2$. *Appl. Phys. Lett.*, **24**, 227.

37 Wagner, S., Shay, J.L., Migliorato, P., and Kasper, H.M. (1974) $CuInSe_2$/CdS heterojunction photovoltaic detectors. *Appl. Phys. Lett.*, **25**, 434.

38 Shay, J.L., Wagner, S., and Kasper, H.M. (1975) Efficient $CuInSe_2$/CdS Solar Cells. *Appl. Phys. Lett.*, **27**, 89.

39 Repins, I., Contreras, M.A., Egaas, B., DeHart, C., Scharf, J., Perkins, C.L., To, B., and Noufi, R. (2008) 19.9%-efficient ZnO/CdS/$CuInGaSe_2$ solar cell with 81.2% fill factor. *Prog. Photovolt.: Res. Appl.*, **16**, 235.

40 Mickelsen, R.A. and Chen, W.S. (1980) High photocurrent polycrystalline thin-film CdS/$CuInSe_2$ solar cell. *Appl. Phys. Lett.*, **36**, 371–373.

41 Gabor, A.M., Tuttle, J.R., Albin, D.S., Contreras, M.A., Noufi, R., Jensen, D.G., and Hermann, A.M. (1994) High-efficiency $CuIn_xGa_{1-x}Se_2$ solar cells from $(In_xGa_{1-x})_2Se_3$ precursors. *Appl. Phys. Lett.*, **65**, 198–200.

42 Binsma, J.J.M. and Van der Linden, H.A. (1982) Preparation of thin $CuInS_2$ films via a two-stage process. *Thin Solid Film.*, **97**, 237–243.

43 Probst, V., Karg, F., Rimmasch, J., Riedl, W., Stetter, W., Harms, H., and Eibl, O. (1996) Advanced stacked elemental layer progress for Cu(InGa)Se_2 thin film photovoltaic devices. *Mater. Res. Soc. Symp. Proc.*, **426**, 165–176.

44 Stolt, L., Hedström, J., Kessler, J., Ruckh, M., Velthaus, K.O., and Schock, H.W. (1993) ZnO/CdS/$CuInSe_2$ thin-film solar cells with improved performance. *Appl. Phys. Lett.*, **62**, 597–599.

45 Holz, J., Karg, F., and v. Phillipsborn, H. (1994) The effect of substrate impurities on the electronic conductivity in CIGS thin films. Proc. 12th. European Photovoltaic Solar Energy Conf., Amsterdam, H. S. Stephens & Associates, Bedford, pp. 1592–1595.

46 Nakada, T., Iga, D., Ohbo, H., and Kunioka, A. (1997) Effects of sodium on Cu(In,Ga)Se_2-based thin films and solar cells. *Jpn. J. Appl. Phys.*, **36**, 732–737.

47 Rocket, A. (2005) The effect of Na in polycrystalline and epitaxial single-crystal $CuIn_{1-x}Ga_xSe_2$. *Thin Solid Films*, **480**, 2–7.

48 Siebentritt, S., Igalson, M., Persson, C., and Lany, S. (2010) The electronic structure of chalcopyrite-bands, point defects and grain boundaries. *Progr. Photovolt. Res. Appl.* (published online, doi: 10.1002/pip.936)

49 Dirnstorfer, I., Wagner, M., Hofmann, D.M., Lampert, M.D., Karg, F., and Meyer, B.K. (1998) Characterization of CuIn(Ga)Se_2 thin films – II. In-rich layers. *phys. status solidi (a)*, **168**, 163–175.

50 Bauknecht, A., Siebentritt, S., Albert, J., and Lux-Steiner, M.C. (2001) Radiative recombination via intrinsic defects in $Cu_xGa_ySe_2$. *J. Appl. Phys.*, **89**, 4391–4400.

51 Rau, U., Schmitt, M., Parisi, J., Riedl, W., and Karg, F. (1998) Persistent photoconductivity in Cu(In,Ga)Se_2 heterojunctions and thin films prepared by sequential deposition. *Appl. Phys. Lett.*, **73**, 223–225.

52 Lany, S. and Zunger, A. (2008) Intrinsic DX centers in ternary chalcopyrite semiconductors. *Phys. Rev. Lett.*, **100**, 016401.

53 Rau, U., Taretto, K., and Siebentritt, S. (2009) Grain boundaries in Cu(In,Ga)$(Se,S)_2$ thin-film solar cells. *Appl. Phys. A*, **96**, 221–234.

54 Schmid, D., Ruckh, M., Grunwald, F., and Schock, H.W. (1993) Chalcopyrite/defect chalcopyrite heterojunctions on basis of $CuInSe_2$. *J. Appl. Phys.*, **73**, 2902–2909.

55 Morkel, M., Weinhardt, L., Lohmüller, B., Heske, C., Umbach, E., Riedl, W., Zweigart, S., and Karg, F. (2001) Flat conduction-band alignment at the CdS/$CuInSe_2$ thin-film solar-cell heterojunction. *Appl. Phys. Lett.*, **79**, 4482–4484.

56 Dullweber, T., Hanna, G., Rau, U., and Schock, H.W. (2001) A new approach to high-efficiency solar cells by band gap

grading in $Cu(In,Ga)Se_2$ chalcopyrite semiconductors. *Sol. Energy Mater. Sol. Cells*, **67**, 1–4.

57 Turcu, M., Pakma, O., and Rau, U. (2002) Interdependence of absorber composition and recombination mechanism in Cu(In, Ga)$(Se,S)_2$ heterojunction solar cells. *Appl. Phys. Lett.*, **80**, 2598–2600.

58 Kötschau, I.M. and Schock, H.W. (2003) Depth profile of the lattice constant of the Cu-poor surface layer in $(Cu_2Se)_{1-x}(In_2Se_3)_x$, evidenced by grazing incidence X-ray diffraction. *J. Phys. Chem. Sol.*, **64**, 1559–1563.

59 Nguyen, Q., Orgassa, K., Koetschau, I., Rau, U., and Schock, H.W. (2003) Influence of heterointerfaces on the performance of $Cu(In,Ga)Se_2$ solar cells with CdS and $In(OH_x,S_y)$ buffer layers. *Thin Solid Film.*, **431**, 330–334.

60 Weinhardt, L., Heske., C., Umbach, E., Niesen, T.P., Visbeck, S., and Karg, F. (2004) Band alignment at the i-ZnO/CdS interface in $Cu(In,Ga)(S,Se)_2$ thin-film solar cells. *Appl. Phys. Lett.*, **84**, 3175–3177.

61 Hariskos, D., Spiering, S., and Powalla, M. (2005) Buffer layers in $Cu(In,Ga)Se_2$ solar cells and modules. *Thin Solid Film.*, **480**, 99–109.

62 Nakada, T. and Mizutani, M. (2002) 18% efficiency Cd-free $Cu(In, Ga)Se_2$ thin-film solar cells fabricated using chemical bath deposition (CBD)-ZnS buffer layers. *Jpn. J. Appl. Phys.*, **41**, L165–L167.

63 Hariskos, D., Fuchs, B., Menner, R., Naghavi, N., Hubert, C., Lincot, D., and Powalla, M. (2009) The Zn(S,O,OH)/ZnMgO buffer in thin-film $Cu(In,Ga)(Se,S)_2$-based solar cells part II: Magnetron sputtering of the ZnMgO buffer layer for in-line co-evaporated Cu $(In,Ga)Se_2$ solar cells. *Prog. Photovolt. Res. Appl.*, **17**, 479–488.

64 Cusano, D.A. (2010) CdTe solar cells and photovoltaic heterojunctions in II–VI compounds. *Solid State Electron.*, **6**, 217.

65 Bonnet, D. (2004) The evolution of the CdTe thin film solar cell. Proc. Europ. Photov. Sol. Ener. Conf., Paris, June 2004. WIP Renewable Energies, Munich, p. 1657.

66 Bonnet, D. and Rabenhorst, H. (1972) New results on the development of a thin film p-CdTe/n-CdS heterojunction solar cell. Proc. 9th IEEE Photov. Spec. Conf., Silver Springs, MD, May 1972. IEEE, New York.

67 Wu, X., Keane, J.C., Dhere, R.G., DeHart, C., Duda, A., Gessert, T.A., Asher, S., Levi, D.H., and Sheldon, P. (2001) 16.5%-efficient CdS/CdTe polycrystalline thin-film solar cell. Proc. 17th Europ. Photov. Sol. Energy Conf. Munich, October 2001. WIP Renewable Energies, Munich, p. 995.

68 McCandless, B.E., Qu, Y., and Birkmire, R.W. (1994) A treatment to allow contacting CdTe with different conductors. Proc. 24th IEEE Photov. Spec. Conf., pp. 107–110.

69 Moutinho, H.R., Al-Jassim, M.M., Levi, D.H., Dippo, P.C., and Kazmerski, L.L. (1998) Effects of $CdCl_2$ treatment on the recrystallization and electro-optical properties of CdTe thin films. *J. Vac. Sci. Technnol.*, **16**, 1251–1257.

70 Dobson, K.D., Visoly-Fischer, I., Hodes, G., and Cahen, D. (2000) Stability of CdTe/CdS thin-film solar cells. *Sol. Energy Mater. Sol. Cells*, **62**, 295–325.

71 Romeo, N., Bosio, A., Canevari, V., and Podesta, A. (2005) Recent progress on CdTe/CdS thin film solar cells. *Sol. Energy*, **77**, 795–801.

72 Bätzner, D.L., Romeo, A., Zogg, H., Tiwari, A.N., and Wendt, R. (2000) *Thin Solid Films*, **361–362**, 463–467.

73 Fritsche, J., Kraft, D., Thissen, A., Mayer, T., Klein, A., and Jaegermann, W. (2002) Band energy diagram of CdTe thin film solar cells. *Thin Solid Film.*, **403–404**, 252–257.

74 Visoly-Fisher, I., Cohen, S.R., Gartsman, K., Ruzin, A., and Cahen, D. (2006) Understanding the beneficial role of grain boundaries in polycrystalline solar cells from single-grain-boundary scanning probe microscopy. *Adv. Funct. Mater.*, **16**, 649–660.

75 Pieters, B.E., Stiebig, H., Zeman, M., and van Swaaij, R.A.C.M. (2009) Determination of the mobility gap of μc-Si: H in pin solar cells. *J. Appl. Phys.*, **105**, 044502.

76 Street, R.A. (1991) *Hydrogenated Amorphous Silicon*, Cambridge University Press, Cambridge, pp. 363–403.

77 Chapin, D.M., Fuller, C.S., and Pearson, G.L. (1954) A new silicon p–n junction photocell for converting solar radiation into electrical power. *J. Appl. Phys.*, **25**, 676.

78 Carlson, D.E. and Wronski, C.R. (1976) Amorphous silicon solar cell. *Appl. Phys. Lett.*, **28**, 671.

79 Chittick, R.C., Alexander, J.H., and Sterling, H.F. (1969) The preparation and properties of amorphous silicon. *J. Electrochem. Soc.*, **116**, 77.

80 Spear, W.E. and LeComber, P.G. (1975) Substitutional doping of amorphous silicon. *Solid State Commun.*, **17**, 1193.

81 Zeman, M. (2006) Advanced amorphous silicon solar cell technology, in *Thin Film Solar Cells – Fabrication, Characterization and Applications* (eds J. Poortmans and V. Arkhipov) John Wiley & Sons, Ltd, Chichester, UK, p. 204.

82 Staebler, D.L. and Wronski, C.R. (1977) Reversible conductivity changes in discharge-produced amorphous Si. *Appl. Phys. Lett.*, **31**, 292.

83 de Walle, C.G.V. and Street, R.A. (1995) Silicon–hydrogen bonding and hydrogen diffusion in amorphous silicon. *Phys. Rev. B.*, **51**, 10615.

84 Stutzmann, M., Jackson, W.B., and Tsai, C.C. (1986) Annealing of metastable defects in hydrogenated amorphous silicon. *Phys. Rev. B.*, **34**, 63.

85 Powell, M.J., Deane, S.C., and Wehrspohn, R.B. (2002) Microscopic mechanisms for creation and removal of metastable dangling bonds in hydrogenated amorphous silicon. *Phys. Rev. B*, **66**, 155212.

86 Branz, H. (1999) Hydrogen collision model: Quantitative description of metastability in amorphous silicon. *Phys. Rev. B*, **59**, 5498.

87 Veprek, S., Marecek, V., and Anna Selvan, J.A. (1968) The preparation of thin layers of Ge and Si by chemical hydrogen plasma transport. *Solid State Electron.*, **11**, 683.

88 Usui, S. and Kikuchi, M. (1979) Properties of heavily doped GD-Si with low resistivity. *J. Non-Cryst. Sol.*, **34**, 1.

89 Kroll, U., Meier, J., Keppner, H., Littlewood, S.D., Kelly, I.E., Giannoulès, P., and Shah, A. (1995) Origin and incorporation mechanism for oxygen contaminants in a-Si:H and mc-Si:H films prepared by the very high frequency (70MHz) glow discharge technique. *Mater. Res. Soc. Symp. Proc.*, **377**, 39.

90 Kroll, U., Meier, J., Keppner, H., Littlewood, S.D., Kelly, I.E., Giannoulès, P., and Shah, A. (1995) Origins of atmospheric contamination in amorphous silicon prepared by very high frequency (70MHz) glow discharge. *J. Vac. Sci. Technol. A*, **13**, 2742.

91 Torres, P., Meier, J., Flückiger, R., Kroll, U., Selvan, J.A.A., Keppner, H., Shah, A., Littlewood, S.D., Kelly, I.E., and Giannoulès, P. (1996) Device grade microcrystalline silicon owing to reduced oxygen contamination. *Appl. Phys. Lett.*, **69**, 1373.

92 Meier, J., Dubail, S., Flückiger, R., Fischer, D., Keppner, H., and Shah, A. (1994) Intrinsic microcrystalline silicon – a promising new thin film solar cell material. Proc. 1st World Conf. Photov. Energy Conv., Hawai, p. 409.

93 Flückiger, R. (1995) Microcrystalline silicon thin-films deposited by VHF Plasma for solar cell applications. Ph.D. thesis, Institute of Microtechnology, University of Neuchatel.

94 Green, M.A. (2001) Third generation photovoltaics: ultra-high conversion efficiency at low cost. *Prog. Photovolt. Res. Appl.*, **9**, 123.

95 Henry, C.H. (1980) Limiting efficiencies of ideal single and multiple energy gap terrestrial solar cells. *J. Appl. Phys.*, **51**, 4494.

96 de Vos, A. (1980) Detailed balance limit of the efficiency of tandem solar cells. *J. Phys. D: Appl. Phys.*, **13**, 839.

97 Coutts, T.J., Ward, J.S., Young, D.L., Emery, K.A., Gessert, T.A., and Noufi, R. (2003) Critical issues in the design of polycrystalline, thin-film tandem solar cells. *Prog. Photovolt. Res. Appl.*, **11**, 359.